# Comprehensive numerical model for cw vertical-cavity surface-emitting lasers

G. R. Hadley , K. L. Lear, M. E. Warren, and K. D. Choquette

Sandia National Laboratories
Albuquerque, New Mexico 87185-5800

J. W. Scott

Optical Concepts, Incorporated
432A Commerce Court
Lompoc, CA 93436

S. W. Corzine

University of California at Santa Barbara
Santa Barbara, CA 93106

## ABSTRACT

We present a comprehensive numerical model for vertical-cavity surface-emitting lasers that includes all major processes effecting cw operation of axisymmetric devices. In particular, our model includes a description of the 2D transport of electrons and holes through the cladding layers to the quantum well(s), diffusion and recombination processes of these carriers within the wells, the 2D transport of heat throughout the device, and a multi-lateral-mode effective index optical model. The optical gain aquired by photons traversing the quantum wells is computed including the effects of strained band structure and quantum confinement. We employ our model to predict the behavior of higher-order lateral modes in proton-implanted devices, and to provide an understanding of index-guiding in devices fabricated using selective oxidation.

## 1.INTRODUCTION

Vertical-cavity surface-emitting lasers (vcsels) are presently the subject of intense research due to their promise as compact, efficient laser sources for a number of important applications. Interest in these devices has been spurred by recent advances in output power[1], efficiency[2,3], and the extension of operating wavelengths into the visible[4]. These advances, coupled with inherent advantages such as astigmatic output and epitaxially-grown cavities, are placing vcsels in a potentially competitive position relative to edge-emitting lasers for the first time. However, further optimization of vcsel designs will require more elaborate models that are capable of including the many interdependent processes occuring within the device structure.

In this paper we present such a model for the purpose of understanding the complex physical processes governing cw vcsel operation, with the ultimate goal of producing a numerical simulation tool capable of designing more efficient and useful devices. In particular, our model includes the following physical processes modeled in 2D axisymmetric geometry: (1) The Ohmic transport of carriers through the cladding layers to a quantum well(s), including anisotropic conductivities, (2) The transport of heat towards a heat sink, including source terms from Ohmic dissipation, non-radiative recombination and reabsorbed laser radiation, (3) The diffusion of carriers inside the quantum well(s), and their recombination via spontaneous emission, stimulated emission, and non-radiative processes (both through traps and Auger transitions), (4) The cw behavior of five different optical cavity modes, delineated by their azimuthal dependence, and (5) The interaction of each of these modes with carriers in the quantum well through a comprehensive gain model that includes effects arising from the strained band structure usually present in the quantum wells. We further validate our model through comparison of predicted performance with measured results for two different types of vcsels: (1) gain-guided devices fabricated by ion-implantation, and index-guided devices fabricated using selective oxidation.

Most previous vcsel models[5-8] have concentrated on overall device behavior such as threshold and quantum efficiency using simplified treatments of current and heat flow. Such models typically neglect lateral dependencies, due to the obvious difficulty of calculating the two-dimensional transport, and utilize empirical methods to treat only a few aspects of device behavior. More

# DISCLAIMER

**Portions of this document may be illegible in electronic image products. Images are produced from the best available original document.**

recently, new models have been reported that attempt a more comprehensive approach. Piprek et al.[9] perform elaborate 2D carrier and heat transport calculations, but neglect all lateral waveguiding effects. Zhang and Petermann[10] employ a more complete radially-dependent optical model for a single lateral mode, but restrict their carrier and heat transport analysis with the use of simple analytic formulas that are invalid above threshold. Shimizu et. al.[11] utilize a two-lateral-mode beam propagation optical model and include gain saturation, but do not treat carrier and heat transport through the cladding layers. Thode et. al.[12] have presented the most comprehensive model to date, including fully time-dependent three-dimensional optical, carrier and heat transport models. This very ambitious model is aimed primarily at transient device behavior, and requires extensive mainframe computer resources to implement. The present model concentrates on the phenomena most influential in cw operation, and includes the major physical processes in a self-consistent manner, while requiring modest computer resources (The results reported here were obtained on an IBM RS/600 model 590 workstation).

## 2.MATHEMATICAL MODEL

Transport processes occuring in the vcsel to be simulated are modeled using the rectangular domain shown in Fig. 1(a). Carriers flow from arbitrarily-tailored contacts through the substrate and cladding layers to the active region, ususally composed of one or more quantum wells. Carriers residing in the wells may then diffuse laterally and undergo various recombination processes, while providing gain to the optical cavity modes. Heat is generated within the device, both due to Ohmic heating of carriers during transport and also due to non-radiative processes occuring in the quantum well, as well as reabsorbed radiation. This heat then flows towards a heat sink located either below the substrate or adjacent to the p-cladding layers as shown. The transport of these quantities
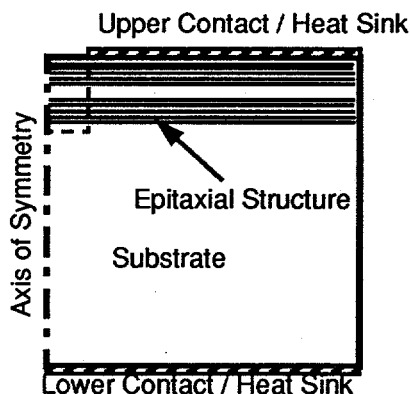


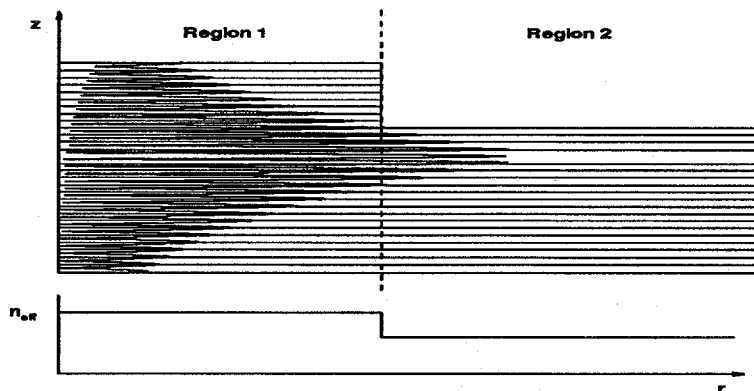Fig. 1(a) Domain geometry used for calculating the transport of carriers and heat



Fig. 1(b) Blowup of the dashed region from Fig 1(a). This is the domain used for the optical model. The latter employs its own mesh, that can be arbitrarily located within the transport mesh.

is computed in the large (~100 μm x 100 μm) domain shown in Fig. 1(a) using a non-uniform mesh. This domain is kept large so as to adequately treat the spreading of both current and heat as it moves toward the bottom of the substrate.

Optical activity, on the other hand, occurs on a more limited spatial scale that is confined to the dashed region shown in Fig. 1(a). The optical field (Fig. 1(b)) is confined vertically by the mirror stacks and laterally by either gain or index guiding. The resulting field is computed on a smaller domain using a separate (and much finer) optical mesh that may be located arbitrarily with respect to the transport mesh. Solution of the optical fields is obtained using an effective index method (as shown schematically in the figure for the case of an etched air-post device) and described in detail below.

The various processes described above are interdependent to varying degrees, thus requiring a highly self-consistent model if accurate predictions are to be obtained. Many of these interdependencies are included in the present model. Perhaps the strongest of these is gain saturation, which links carrier transport in the quantum well (the quantum well diffusion model) with the optical model. In addition, the optical model and the heat transport model are linked through thermal lensing and reabsorbed laser radiation. One could also add the effects of band filling on the carrier transport through the cladding layers, but this effect has not been included at present.

## 2.1 Heat and Carrier Transport

The steady state transport of charge carriers and heat throughout the device is assumed to be linear in nature and thus satisfy the general Poisson Equation

$$\nabla \cdot \overline{\kappa} \nabla \psi = S \tag{1}$$

where the tensor $\overline{\kappa}$ describes the spatially variable transport properties of the materials, $\psi$ is the transported field quantity, and $S$ is the source. For the heat equation, $S$ is the heat source and $\overline{\kappa}$ the thermal conductivity tensor, assumed to be independent of the temperature $\psi$. For the carrier transport equation, $S$ is zero and $\overline{\kappa}$ is the electrical conductivity tensor, that once again is assumed to be independent of the potential $\psi$. The transport of carriers is also known to depend upon a variety of nonlinear effects, such as thermionic emission, in the vicinity of material interfaces. We will not attempt a detailed treatment of these effects, but rather model transport in the directions normal to and parallel to the interfaces of the DBR mirrors using Eq. (1) together with anisotropic average electrical conductivities.

The appropriate source term $S$ for the heat equation describes several different heat generation mechanisms, including Ohmic heating by carriers, dissipitative recombination processes in the quantum wells, and the reabsorption of both laser and spontaneously-emitted radiation. We include all but the last effect in our treatment, due to the difficulty of calculating its spatial dependence, together with the knowledge that it is relatively diffuse in comparison with the other more concentrated sources[13].

We solve a finite-differenced form of Eq. (1) inside a rectangular region of the $r$-$z$ plane using an iterative ADI procedure[14] that allows mixed boundary conditions to facilitate the simulation of more general heat sink and contact geometries. Internal transport barriers such as implanted regions are modeled by locally decreasing the value of the transport tensor.The finite difference equations we employ are conservative in form and derived starting from an integrated form of Eq. (1).

Obtaining the solution of the above general carrier transport equation results in a knowledge of the current density $J(r)$ impinging upon the active region. Carriers thus arriving at the active region are assumed to diffuse radially within the quantum wells and recombine in a manner described by the one-dimensional nonlinear ambipolar diffusion equation

$$\frac{D}{r}\frac{d}{dr}\left(r\frac{dN}{dr}\right) = -\frac{J(r)}{qd} + \frac{N(r)}{\tau_{nr}} + BN^2 + CN^3 + \frac{g_{eff}(r)}{h\nu d}\sum_{m=1}^{M}|E_m(r)|^2 \tag{2}$$

where $N$ is the density of electrons and holes in the quantum well, $D$ is the (constant) diffusion coefficient, $q$ the magnitude of the electronic charge, $d$ the effective quantum well width (the total width for multiple quantum wells), $\tau_{nr}$ the nonradiative recombination time, $B$ the coefficient for spontaneous emission, $C$ the Auger coefficient, $h\nu$ the photon energy, and $g_{eff}$ the effective gain coefficient. The latter depends on radius through its dependence upon carrier density, lasing wavelength and temperature via an elaborate gain model to be described in a later section. The lasing intensity term is summed incoherently over all lateral modes present, since each lases at a different frequency.

We produce a finite-differenced form of Eq. (2) by premultiplication by $r$ and integration over the range $r_{i-\frac{1}{2}}$ to $r_{i+\frac{1}{2}}$. This equation is then linearized by expansion about the previous solution at each mesh point. The resulting linear equation is then solved using the Thomas tridiagonal algorithm and the iterative process repeated until convergence is obtained. Due to the strong non-linearities involved, under-relaxation is used to prevent gain overshoot and undershoot.

## 2.2 Optical Model

Lasing modes in a vertical cavity laser are characterized by near-paraxial propagation normal to the mirror layers, with polarizations in the plane of the mirrors. Under these conditions only a single electric field component is appreciable, and we may describe that field adequately with the scalar wave equation

$$\nabla^2 E - \frac{\varepsilon}{c^2}\frac{\partial^2 E}{\partial t^2} = 0 \tag{3}$$

where $\varepsilon$ is the relative permitivity and we have assumed the relative permeability to be unity. Since $E$ depends on all three spatial coordinates and time, we cannot easily solve Eq. (3) for a complicated structure such as a vcsel. Instead, we invoke two simplifying assumptions: (1) that the time dependence is nearly harmonic with (complex) frequency $\omega_0$, and (2) that the vcsel structure depends only upon $z$ within each of a number of concentric cylindrical regions. Thus we write for region $i$,

$$E(r, z, \phi, t) \approx \varphi_i(z) E(r, \phi, t) e^{-i\omega_0 t} \tag{4}$$

Substituting (4) into (3) and writing $\nabla^2 = \frac{\partial^2}{\partial z^2} + \nabla_t^2$ results in

$$\varphi_i'' E + \varphi_i \nabla_t^2 E + \varepsilon k_0^2 \varphi_i E + 2i\varepsilon k_0 \varphi_i \frac{\partial E}{\partial \tau} = 0 \tag{5}$$

where we have introduced the vacuum wavevector $k_0 \equiv \frac{\omega_0}{c}$ and the modified time coordinate $\tau \equiv ct$, and have invoked the slowly-varying envelope approximation by neglecting second derivatives with respect to time when acting on the function $E$. In anticipation of the separability assumption, we next write the relative permitivity as the sum of a structural component $\varepsilon_i$ and a non-structural component $\varepsilon_g$ that is expected to include such effects as radially-dependent gain in the quantum well, and thermal lensing:

$$\varepsilon(r, z) \equiv \varepsilon_i(z) + \varepsilon_g(r) \tag{6}$$

At this point we introduce the effective index approximation by assuming that (1) the functions $\varphi_i$ each satisfy a one-dimensional eigenvalue equation of the form

$$\varphi_i'' + k_0^2 (1 - \xi_i) \varepsilon_i(z) \varphi_i = 0 \tag{7}$$

where the complex eigenvalue $\xi_i$ is related to the effective index, and (2) that the eigenfunctions $\varphi_i$ are all approximately identical in each of the distinct problem regions, so that $\varphi_i(z) \approx \varphi_j(z) \equiv \varphi(z)$. The latter statement embodies the essence of the effective index method by implying approximate separability, with the dominant effect of structure variations appearing primarily as a variation in the effective index.

If we now use Eq. (7) to eliminate the $\varphi''$ term in Eq. (5), we have

$$k_0^2 (\varepsilon_g(r) + \xi \varepsilon_i(z)) \varphi E + \varphi \nabla_t^2 E + 2ik_0 \varepsilon_i(z) \varphi \frac{\partial E}{\partial \tau} = 0 \tag{8}$$

The $z$-dependence in Eq. (8) may be removed by multiplying by $\varphi^*$ and integrating over $z$, resulting in

$$k_0^2 (\langle \varepsilon_g \rangle + \xi \langle \varepsilon_i \rangle) E + \nabla_t^2 E + 2ik_0 \langle \varepsilon_i \rangle \frac{\partial E}{\partial \tau} = 0 \tag{9}$$

where we have defined

$$\langle \varepsilon_i \rangle \equiv \frac{\int \varphi^* \varepsilon_i(z) \varphi \, dz}{\int \varphi^* \varphi \, dz} \tag{10}$$

Eq. (9) may be rewritten in the form of a beam propagation equation where the propagation direction is the time-like variable $\tau = ct$. The result is

$$\frac{\partial E}{\partial \tau} = \frac{i}{2k_0 \langle \varepsilon_i \rangle} (\nabla_t^2 + k_0^2 \Delta \varepsilon_{\text{eff}}) E \tag{11}$$

where we have defined the variation in effective dielectric constant as $\Delta \varepsilon_{\text{eff}} \equiv \langle \varepsilon_g \rangle + \xi_i \langle \varepsilon_i \rangle$ and $\langle \varepsilon_g \rangle$ is given by

$$\langle \varepsilon_g \rangle = 2\sqrt{Re(\langle \varepsilon_i \rangle)} \frac{dn}{dT} (\langle T \rangle(r) - T_0) - \frac{ign_a \langle u \rangle}{k_0} \tag{12}$$

where $\frac{dn}{dT}$ is the derivative of the refractive index with respect to temperature, $g$ and $n_a$ are the material gain coefficient and index of refraction of the quantum wells, and $u$ is a function that is unity in the quantum wells and zero otherwise. We have ignored

changes in refractive index due to the presence of carriers in Eq. (12), because the small value of $\langle u \rangle$ renders those changes small ($\sim 5 \times 10^{-4}$) compared with those due to thermal lensing ($\sim 5 \times 10^{-3}$).

Note that despite the familiar form of Eq. (11), it is in reality an expression of time variation, so that the model we are espousing is *not* a true beam propagation model. This distinction is clarified by the observation that in our model there is no necessity of defining an effective mirror penetration depth, as is the case with true beam propagation models[11]. This is of considerable advantage for calculating the losses incurred, for example, by free carrier absorption resulting from mirrors grown using arbitrary doping profiles. The inclusion of such losses is awkward with a beam propagation approach, but appears naturally in our model as a contribution to the imaginary part of the eigenvalue $\xi_i$.

Our optical model thus consists of two parts: (1) initial solutions of Eq. (7) for each region that result in the eigenvalues $\xi_i$, and (2) Iterative solutions of Eq. (11) for each lateral mode that continue until both the radial dependence and magnitude of $E$ (proportional to the square root of the recirculating power) cease to change. Different lateral modes are defined by requiring cylindrical symmetry for the field $E$. Thus $E$ must be of the form

$$E(r, \phi, t) \equiv E_m(r, t) e^{\pm im\phi} \tag{13}$$

Inserting Eq. (13) into Eq. (11) and writing the Laplacian in cylindrical coordinates results in the following propagation equation for the $m^{th}$ lateral mode:

$$\frac{\partial E_m}{\partial \tau} = \frac{i}{2k_0 \langle \varepsilon_i \rangle} \left( \frac{1}{r} \frac{\partial}{\partial r} r \frac{\partial}{\partial r} - \frac{m^2}{r^2} + k_0^2 \Delta\varepsilon_{eff} \right) E_m \tag{14}$$

Up to this point all field expressions have been written in such a way as to be independent of normalization. The latter must however be determined consistently with the stimulated emission term in Eq. (2) so that the recombination of one electron-hole pair produces exactly one photon. This condition is properly met if we define the effective gain coefficient in Eq. (2) as

$$g_{eff} \equiv \frac{n_a g \langle u \rangle}{k_0 Re(\langle \varepsilon_i \rangle)} \tag{15}$$

and the radiated output power density by

$$P_{out} \equiv Im(\xi_i) \Big|_{rad} |E|^2 \tag{16}$$

with

$$Im(\xi_i) \Big|_{rad} = \frac{n_u |\varphi_i|^2_u}{k_0 Re(\langle \varepsilon \rangle) \int \varphi_i^* \varphi_i \, dz} + \frac{n_l |\varphi_i|^2_l}{k_0 Re(\langle \varepsilon \rangle) \int \varphi_i^* \varphi_i \, dz} \tag{17}$$

and the subscripts u and l referring to the material above and below the mirror stack, respectively. With the above choice of normalization, $|E|^2$ is proportional to the recirculating power density, having units of W/cm$^2$. We note in passing that the expression for the effective gain coefficient in Eq. (15) is a weighted average and therefore automatically accounts for resonant-periodic-gain effects, yielding zero gain if the quantum well is placed exactly at a field node.

## 2.3 Gain model

The material gain coefficient $g\,(N, \lambda, T)$ appearing in Eq. (12) is determined from detailed band structure calculations for the 8-nm-wide compressively-strained $In_{0.2}Ga_{0.8}As$ quantum wells. The details of these calculations have been reported elsewhere[16,17], and will be briefly summarized here for the sake of completeness. Due to the level of sophistication of these calculations, they are performed only once for a given quantum well structure with the results being stored in look-up tables or fitted by analtyic functions. These tables or functions are then employed in the vcsel simulations.

These calculations begin with a determination of the subband structure of the strained quantum well for both conduction and valence bands. The quantized subband edge energy levels in both bands are determined by solving Schroedinger's Equation with a finite barrier potential appropriate for the $In_{0.2}Ga_{0.8}As/GaAs$ system ($E_G$(GaAs:C-HH,LH) = 1.424 eV and $E_G$($In_{0.2}Ga_{0.8}As$:strained C-HH)=1.215 eV with 60% of the bandgap discontinuity assumed to appear in the conduction band). In the valence band, a different potential well is seen by heavy and light holes due to strain[16]. The three potential well depths used are: $V_C$=125 meV, $V_{HH}$=83.6 meV, and $V_{LH}$=3.75 meV (due to the strain-induced splitting of the heavy and light hole bands, the light holes are nearly unconfined). The resulting quantized energies in the quantum well are: $E_{Cn}$=37.4,122, $E_{HHn}$=9.61,37.3,76.2, and $E_{LHn}$=83.1, all in meV.

The next step involves determing the subbands associated with each quantized energy level. In the conduction band, each subband is assumed to be parabolic in our model, with an in-plane effective mass that is a weighted average of the band edge conduction band effective masses in and out of the well (0.059 $m_0$ and 0.067 $m_0$, resp.). In the valence band, a realistic model must account for the complex interactions between the heavy and light hole subbands which lead to subband warping. To include these valence band-mixing effects, the Luttinger-Kohn (L-K) Hamiltonian[18] is employed. In our model we use the 4x4 version of the L-K Hamiltonian that takes into account the coupling between the heavy and light hole valence bands, but neglects the coupling to the split-off band (aside from strain shifts in the bandgaps that do include split-off band coupling).
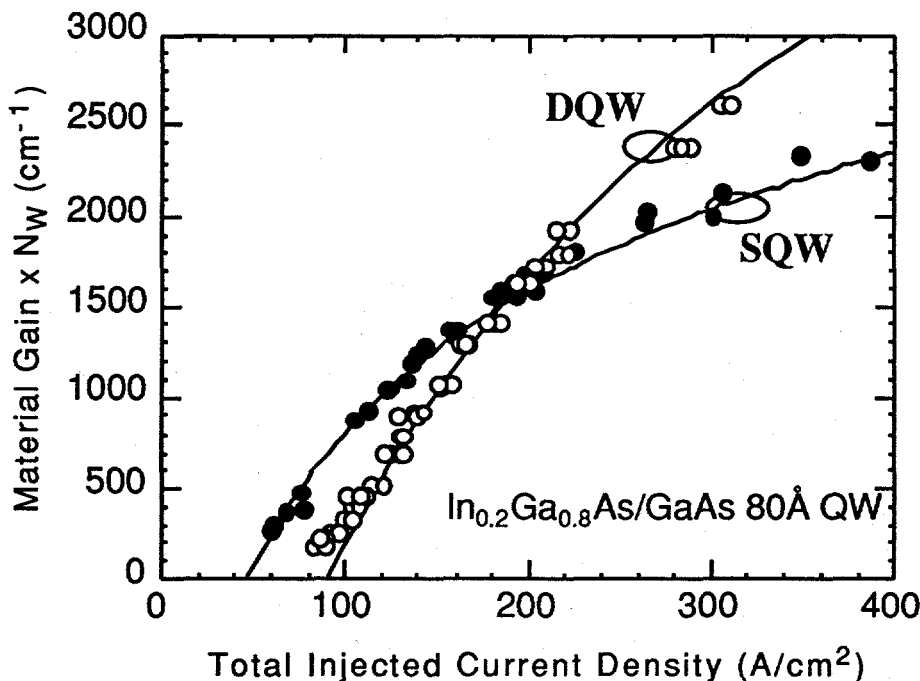


Fig. 2 A comparison between theoretical gain and measured gain (taken from different length devices) as a function of current density in single and double $In_{0.2}Ga_{0.8}As/GaAs$ 8 nm quantum well active region edge-emitting lasers. (After Ref. [22]). Auger and barrier recombination included.

A unity transformation applied to the 4x4 L-K Hamiltonian transforms it into two 2x2 decoupled Hamiltonians, making the analysis much simpler, as first suggested by Broido and Sham[19] (and outlined in more detail by Ahn and Chuang[20]). After adding the strained heavy hole and light hole finite barrier potential well profiles to the L-K Hamiltonian (in a manner equivalent to that described in [20]), we can solve for the quantum well envelope functions. The corresponding energy eigenvalues as a function of in-plane k vector are then found successively, producing the entire valence subband structure.

Once the subband structure is determined, we can concentrate on the more relevant topic of calculating the gain function. To predict the gain/absorption characteristics of quantum well structures in general, we need to know (1) the density of states in both the conduction and valence bands, (2) the interband transition matrix elements, and (3) the quasi-Fermi levels in both bands. With the subband structure results as described above, we can easily calculate the density of states. A knowledge of the envelope functions combined with the strength of the bulk momentum matrix element (for $In_{0.2}Ga_{0.8}As$ we assumed $2|M|^2/m_0 = 27.48$ eV) allow a determination of the interband transition matrix element as a function of in-plane k vector for every subband transition pair[16].

This leaves only the task of determing the quais-Fermi levels in each band. In our model we treat the conduction band quasi-Fermi level as the independent variable of the calculation and relate the valence band quasi-Fermi level to it by invoking charge neutrality in the quantum well region (including "bulk" states at energies beyond the potential barrier heights). With these defined we can uniquely determine the carrier density within each band and the gain/absorption spectrum of the quantum well. Spectral broadening of the transitions is taken into account by convolving the resulting gain spectrum with an energy-dependent line-shape function[21] (it is similar to a Lorentzian with an intraband scattering time of 0.1 psec, with the exception that the function used here is reduced by more than an order of magnitude "in the wings" as compared to the Lorentzian). In this way, the carrier density and broadened gain spectrum can be found as a function of increasing quasi-Fermi level separation.

The resulting gain model has been compared with experiment by integrating the total emission rate over all possible transitions as calculated above, and comparing calculated gain vs. radiative current density with measured values for edge-emitting lasers employing both single and double $In_{0.2}Ga_{0.8}As/GaAs$ 8-nm-wide quantum wells. The resulting comparisons, shown in Fig. 2, are excellent[22], particularly in view of the fact that the calculations employed no fitting parameters.

### 3. COMPARISON WITH EXPERIMENT

We illustrate the use and demonstrate the validity of the model described in this work by comparing model predictions against measured device performance for two different types of vertical cavity lasers. The first is a gain-guided device with no built-in index structure whose lateral mode shape is determined by the shape of the gain profile. The second is an index-guided laser whose index step results from the insertion of a low-index layer formed by wet oxidation of a single AlGaAs mirror layer. This device offers a challenging test of the effective index model described above.

#### 3.1 Gain-guided vcsel

The devices used for this comparison were processed from molecular-beam-epitaxially-grown wafers of AlGaAs mirrors on n-type GaAs substrates with triple InGaAs quantum wells, as described in detail elsewhere[2]. Gain-guided vcsels with circular symmetry and diameters ranging from 10-35 μm were then defined by proton bombardment. We modeled a simplified version of the devices in which the triple quantum wells were assumed to have equal carrier density profiles. The electrical resistivities were modified to reproduce the measured device resistance for several different device diameters. Likewise, the thermal conductivities were modified to reproduce the measured device temperature rise. The latter quantity was determined by observing the Fabry-Perot resonance shift (at zero device current) as the temperature of the mounting stage was varied. This procedure provided not only the relationship between device temperature and emission wavelength, but also the material parameter $dn/dT$, which was found to have a value of $2.3 \times 10^{-4}$. The device was then simulated using the model described in the previous sections and the measured value of $dn/dT$. The resulting predicted LI curves for the 15-μm-diameter device are shown in Fig.3 along with the measured results. The simulation clearly predicts the onset of two higher-order lateral modes at the currents shown. These two modes were also observed experimentally, appearing at currents corresponding to the kinks in the curve marked "Experiment" in Figure 3 (and confirmed by near-field and spectral measurements). In addition, the calculated results accurately predict the measured threshold current and differential quantum efficiency, and approximately predict the observed thermal rollover. Further calculations performed with
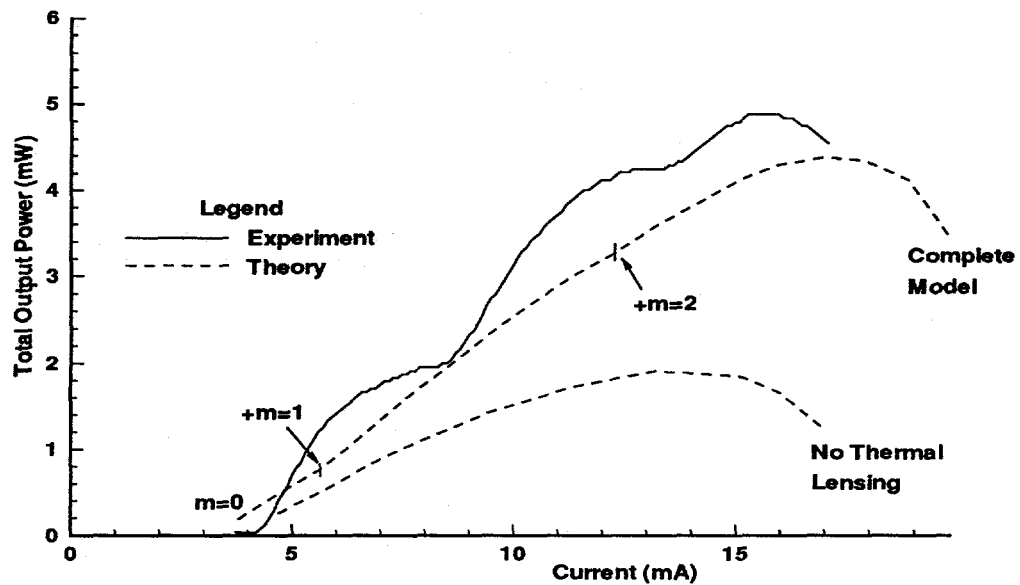
Fig. 3. Comparison between model results and data for the implanted gain-guided device. The model predicts only the fundamental mode at low power, with higher-order lateral modes coming in above threshold at the points shown.
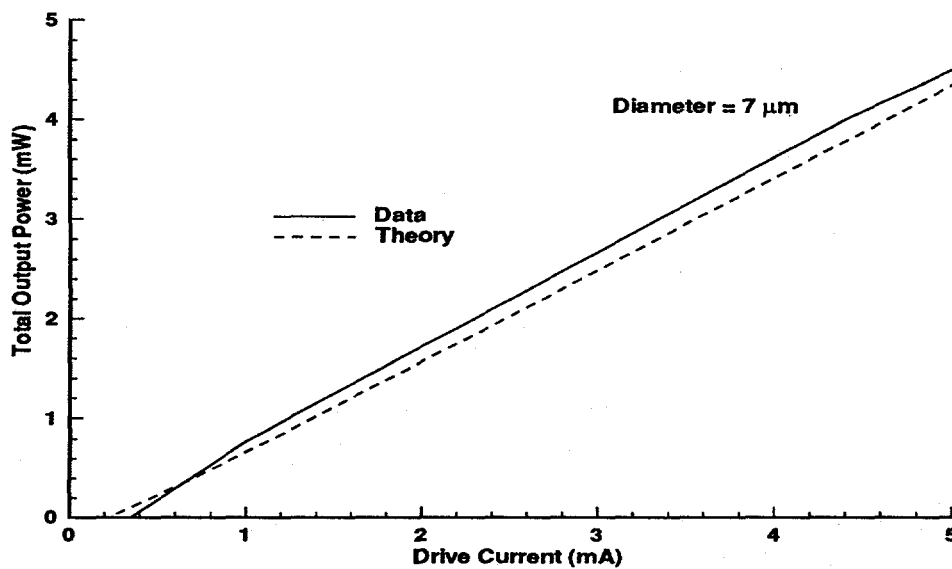


Fig. 4 Measured and predicted LI curves for a 3-mm-diameter index-guided device fabricated by selective oxidation. The model predicts a maximum efficiency of 46%, just below the record value of 50% measured experimentally.

thermal lensing effects removed show a decreased differential quantum efficiency and only a single lateral mode (Fig.3). These results demonstrate clearly the crucial role played by thermal lensing in determining the cw modal behavior of implanted devices. The thermal lens acts to pull the higher-order modes into the gain region, where they compete more effectively with the fundamental mode. It also leads to tighter confinement of the fundamental mode, with the resulting higher efficiency.

### 3.2Index-guided vcsel

Devices used for this study were processed from wafers grown using MOVPE of a design similar to that previously used to make implanted devices. The wafers differed only in the use of fewer upper mirror pairs, and the modification of the Aluminum content of on mirror layer adjacent to the cavity from 96% to 98%. These wafers were processed by first etching large rectangular mesas followed by oxidation as described elsewhere[3]. The slight difference in Al content of the mirror layers resulted in the preferential oxidation of the single 98% layer, and the consequent formation of a current aperture with a rounded rectangular shape of varying dimensions. The lower index of refraction of the oxide layer also results in the reduction of the effective index in the oxidized region of the vcsel as computed using Eq. (7). The magnitude of the resulting index step has been computed to be approximately 0.066, a large enough value to cause highly effective optical confinement. This is also in good agreement with the value of 0.062 inferred from a measurement of lateral mode spacing below threshold[23].
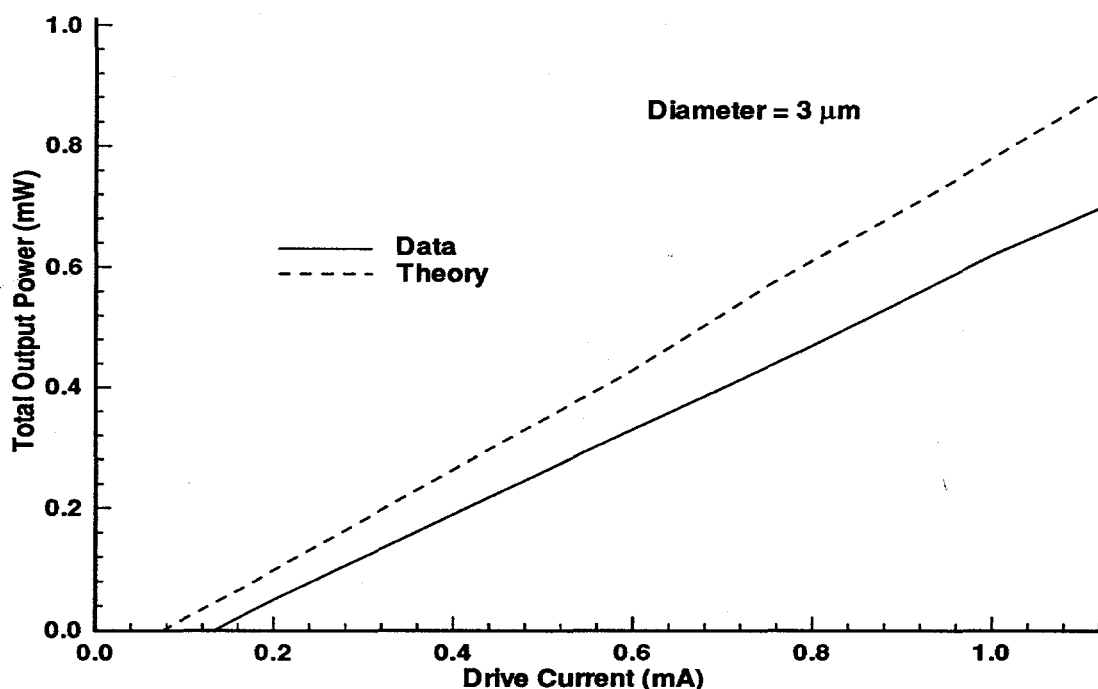


Fig. 5 Measured and predicted LI curves for a 3-mm-diameter index-guided device fabricated by selective oxidation. The measured lower efficiency and higher threshold (as compared with the calculation) are believed to result from an anomalous loss due to the low-index oxide layer not accounted for in the model.

We chose two devices for comparison whose apertures were rounded squares with sides of approximately 3 and 7 μm, and simulated their performance using the model described above as circular devices with radii of 1.5 and 3.5 μm, respectively. The two simulations employed identical properties, with only the oxidation diameter being varied. The resulting measured and calculated LI curves are shown in Figures4 and 5. As can be seen, the 7 μm diameter simulation matches the data very closely, with the predicted threshold (240 μA) slightly under the measured value of 350 μA, and the maximum efficiency (46%) just under the world-record measured efficiency of 50 %. For the 3μm-diameter device, however (see Fig. 5), the simulations predict lower threshold current

and higher quantum efficiency than were measured in the laboratory. It thus appears that the oxide layer is introducing an extra loss into the cavity that is not being accounted for by the effective index formalism. We believe that this loss is related to the fact that the low-index oxide layer introduces a lumped rather than a distributed index change, a mechanism not predicted by the effective index formalism since the latter describes an average (or distributed) change in index. This inaccuracy in the effective index method for this case corrolates with a failure of the separability assumption that underlies its derivation. Thus we conclude that more accurate modeling of such strongly index guided devices will require a more sophisticated optical model.

## 4.CONCLUSION

In summary, we have presented a comprehensive model for the simulation of vertical-cavity surface-emitting semiconductor lasers that calculates the transport of both heat and carriers as well as the behavior of the multi-lateral-mode optical fields and their interaction with the quantum-well gain region. The resulting model has successfully predicted the threshold currents, output powers and lateral mode behavior of gain-guided vcsels, including thermal rollover effects at high injection currents. Considerable success has also been achieved at predicting and understanding the impact of thermal lensing on the onset of higher-order lateral modes. For the strongly index-guided devices fabricated with selective oxidation, the model still predicts thresholds and efficiencies well for the large diameter (7 μm) case. However, index guiding in these devices results from a single low-index layer. Because this layer strongly perturbs the shape of the field profile, the separability assumption used in the derivation of the effective index equations is violated, leading to inaccuracies in predicted device behavior that are the most noticeable for the small diameter (3 μm) lasers. Accurate predictions of the model behavior of these devices may require a more sophisticated optical model.

## 5.ACKNOWLEDGEMENT

## 6.REFERENCES

1. D. B. Young, J. W. Scott, F. H. Peters, M. G. Peters, M. L. Majewski, B. J. Thibeault, Scott W. Corzine, and Larry A. Coldren, "Enhanced performance of offset-gain high-barrier vertical-cavity surface-emitting lasers", IEEE J. Quantum Elect., Vol. QE-29, No. 6, p2013-2022(1993).

2. K. L. Lear, S. P. Kilcoyne, and S. A. Chalmers, "High power conversion efficiencies and scaling issues for multimode vertical-cavity top-surface-emitting lasers", IEEE Photonics Tech. Lett. Vol. 6, No. 7, p778-781(1994).

3. K. L. Lear, K. D. Choquette, R. P. Schneider, Jr., S. P. Kilcoyne, and K. M. Geib, "Selectively Oxidized Vertical Cavity Surface Emitting Lasers", Electron. Lett. Vol. 31, No. 3(1995).

4. J. A. Lott and R. P. Schneider, Electron. Lett. Vol. 29, p830(1993).

5. J. W. Scott, S. W. Corzine, D. B. Young, and L. A. Coldren, "Modelling the current-to-light characteristics of index-guided vertical-cavity surface-emitting lasers", App. Phys. Lett. Vol. 62, No. 10, p1050-1052(1993).

6. J. W. Scott, R. S. Geels, S. W. Corzine, and L. A. Coldren, "Modelling temperature effects and spatial hole burning to optimize vertical-cavity surface-emitting laser performance", IEEE Journal of Quantum Elect. , Vol. QE-29, No. 5, p1295-1308(1993).

7. W. W. Chow, R. P. Schneider, Jr., J. A. Lott, and K. D. Choquette, "Wavelength dependence of the threshold in an InGaP-InAlGaP vertical cavity surface emitting laser", Appl. Phys. Lett. Vol. 65, No. 2, p135-137(1994).

8. D. I. Babic, R. J. Ram, J. E. Bowers, M. Tan, and L. Yang, "Scaling laws for gain-guided vertical cavity lasers with distributed Bragg reflectors", Appl. Phys. Lett. Vol.64, No.14, p1762-1764(1994).

9. J. Piprek, H. Wenzel and G. Sztefka, "Modeling thermal effects on the light vs. current characteristic of gain-guided vertical-cavity surface-emitting lasers", IEEE Phot. Tech. Lett. Vol. 6, No. 2, p139-142(1994).

10. J.-P. Zhang and K. Petermann, "Beam propagation model for vertical-cavity surface-emitting lasers: threshold properties", IEEE J. Quantum Elect. Vol. QE-30, No. 7, p1529-1536(1994).

11. M. Shimizu, F. Koyama and K. Iga, "Transverse mode analysis for surface emitting laser using beam propagation method", IEICE Transactions, Vol. E 74, No. 10, p3334-3341(1991).

12. L. E. Thode, G. Csanak, L. L. So and T. J. T. Kwan, "Time-dependent numerical simulation of vertical cavity lasers", Proc. SPIE, Symposium on Physics and Simulation of Optoelectronic Devices II, Vol. 2146, p174-184, Jan. 24, 1994 Los Angeles.

13. G. R. Hadley, J. P. Hohimer and A. Owyoung, "Comprehensive modeling of diode arrays and broad-area devices with applications to lateral index tailoring", IEEE J. Quantum Elect., Vol. QE-24, No. 11, p2138-2152(1988).

14. W. H. Press, S. A. Teukolsky, W. T. Vetterling and B. P. Flannery, Numerical Recipes in FORTRAN, Second Edition, Cambridge University Press, 40 West 20th St., New York, NY, p.861.

15. A. E. Siegman, Lasers, University Science Books, Mill Valley, CA, p.430.

16. S. W. Corzine, R. H. Yan and L. A. Coldren, "Optical Gain in III-V Bulk and Quantum Well Semiconductors," chapter 1 of Quantum Well Lasers, ed. P. S. Zory, New York: Academic Press, 1993.

17. S. W. Corzine, R. H. Yan and L. A. Coldren, "Theoretical Gain in Strained InGaAs/AlGaAs Quantum Wells including Valence-Band Mixing Effects," Appl. Phys. Lett. 57, 2835(1990).

18. J. M. Luttinger and W. Kohn, "Motion of Electrons and Holes in Perturbed Fields," Phys. Rev. 97, 869(1955).

19. D. A. Broido and L. J. Sham, "Effective Masses of Holes at GaAs-AlGaAs Heterojunctions," Phys. Rev. B 31,888(1985).

20. D. Ahn and S. L. Chuang, "Optical Gain in a Strained-Layer Quantum-Well Laser," IEEE J. Quantum Elect. QE-24, 2400(1988).

21. S. R. Chinn, P. S. Zory, and A. R. Reisinger, "A Model for GRIN-SCH-SQW Diode Lasers," IEEE J. Quantum Electron. QE-24, 2191 (1988).

22. S. Y. Hu, D. B. Young, S. W. Corzine, A. C. Gossard, and L. A. Coldren, "High Efficiency and Low Threshold InGaAs/AlGaAs Quantum Well Lasers," J. Appl. Phys. 76,3932(1994).

23. K. L. Lear, K. D. Choquette, R. P. Schneider and S. P. Kilcoyne, Submitted to Appl. Phys. Lett..

## DISCLAIMER